Eur. Phys. J. B (2021) 94:129
https://doi.org/10.1140/epjb/s10051-021-00137-4

THE EUROPEAN PHYSICAL JOURNAL B

Regular Article – Solid State and Materials

Photoionization cross-section in a $GaAs$ spherical quantum shell: the effect of parabolic confining electric potentials

Moletlanyi Tshipa[1,a], Lalit K. Sharma[1], and Surender Pratap[2]

[1] University of Botswana, Private Bag 0022, Gaborone, Botswana
[2] Central University of Himachal Pradesh, 176206 Dharamshala, India

Received 6 January 2021 / Accepted 3 June 2021 / Published online 22 June 2021

Abstract. Theoretical study on binding energies due to a centred charged impurity and the associated photoionization cross-section (PCS) in a spherical shell are presented. This was achieved by solving the Schrödinger equation within the effective mass approach. Intrinsic to the spherical quantum shell may be the parabolic potential or the shifted parabolic potential, each superimposed on an infinite spherical square well. Results indicate that the parabolic potential enhances binding energies while the shifted parabolic potential diminishes them. These electric potentials considerably modify photoionization cross section in two ways. One, the parabolic potential blueshifts peaks of PCS while the shifted parabolic potential redshifts the peaks. Second, the parabolic potential decreases the magnitude of the peaks of the PCS while the shifted parabolic potential increases the magnitudes of the peaks. In essence, these two potential may be used to manipulate PCS in quantum structures.

1 Introduction

Nanofabrication techniques such as chemical vapour deposition [1,2], lithography [3,4], molecular beam epitaxy [5,6] and atomic layer deposition [7] (or a combination thereof [8]), have been very instrumental in the realization of nanostructures. These structures have a wide range of applications: in bioscience [9–11], photodetection [12], optoelectronics [13–15], communications [16], energy technology [17–19] and in data storage systems [20]. Another promising avenue is quantum computing [21], wherein computing power and speed can be several orders of magnitude more superior than conventional processors [21].

These structures may contain impurities due to intentional doping [22–24] or due to contamination during the growth processes, or both. Therefore, understanding of effects of impurities on quantum properties of electrons is key, particularly if they are electrically charged. Thus, effect of electric field on binding energies in quantum structures has been investigated [25–27]. Magnetic fields also play a significant role in altering quantum properties of electrons [28], hence their effect on binding energies has been studied in a quantum well [29], quantum dot [30], cylindrical quantum well wires [31,32] and in quantum discs [33]. Because hydrostatic pressure influences the energy band gap, it inevitably modifies the effective mass of an electron in a material, and coupled with the fact that it also alters the dielectric constant, it indubitably influences binding energies [34,35]. Position of the impurities in nanostructures also plays a very significant role in binding energies. In view of this, binding energies due to off-centred impurities have been reported in ellipsoidal quantum dots [36] and in spherical quantum dots [37,38]. In most theoretical investigations that have been reported, the region accessible to electrons is electrostatically homogeneous. However, there are a number of reports on multilayered nanostructures, which offer great insight into the quantum properties of electrons in the vicinity of charged impurities in these structures [39–41].

When an electron is bound to a donor impurity, it can be freed from the electrostatic grasp of the impurity if it is supplied with enough energy. If the source of the supplied energy is light, then the process is known as photoionization. Photoionization cross section (PCS) has been studied both theoretically and experimentally for a number of systems, for example in spherical core/shell quantum dots [42], ellipsoidal core/shell quantum dots [43], cylindrical core/shell nanowires [44] and cones [45], among others. The effects of spatially variant electric potentials on PCS have also been investigated [46,47]. The results indicated that PCS can be tuned, its peaks be redshifted or blueshifted, and the magnitude of PCs can be modulated by use of spatially variant electric confining potentials.

In this paper, photoionization cross-section and binding energies due to a charged impurity in a spheri-

[a] e-mail: tshipam@ub.ac.bw (corresponding author)

cal quantum shell (SQS) are sought for analytically within the effective mass approximation. The electrostatic potentials inside the shell considered here vary parabolically as outlined in the next section. The organizational structure is as follows: The Preliminary notes section is concerned with the theoretical formulation of the problem, whose results and discussions are found in the Results section. Lastly, the concluding remarks are dealt with in the Conclusions section.

2 Preliminary notes

2.1 Photoionization cross-section

Photoionization cross-section can be regarded as the probability that a bound electron can be freed from an electrostatic grasp by assimilating energy ($\hbar\omega$) from a photon of a certain frequency. It is mathematically modelled as [46,47]

$$\sigma_{lm} = \sigma_0 \sum_f |\langle f|\mathbf{r}|i\rangle|^2 \delta(\Delta E - \hbar\omega), \tag{1}$$

where ΔE is energy difference between final state f (associated with energy E_f) and initial state i (with associated energy E_i) and $\mathbf{r}$ is position vector of an electron. Here, $\sigma_0 = (4\pi^2\alpha_{FS} n E_{in}^2 \hbar\omega)/(3\epsilon_m E_{av}^2)$, where E_{in} is amplitude of electric field of incident radiation while E_{av} is the average electric field of the radiation inside the crystal of refractive index n and dielectric constant ϵ_m. α_{FS} ($\approx 1/137$) is the fine structure constant. To aid in the computations, the delta function that conserves energy in Eq. (1) is approximated by the Lorentzian

$$\delta(\Delta E - \hbar\omega) \to \frac{\hbar\Gamma_{fi}}{\pi[(\Delta E - \hbar\omega)^2 + (\hbar\Gamma_{fi})^2]}, \tag{2}$$

where Γ_{fi} is the relaxation rate of the initial and the final states, related to the $|i\rangle \to |f\rangle$ transition lifetime τ_{fi} by $\Gamma_{fi} = 1/\tau_{fi}$.

2.2 Wave functions

The envisaged system is one in which an impenetrable spherical core is surrounded evenly by a semiconductor, all embedded in a glass matrix. A charged impurity situates in the core, and for simplicity, at the center of the core. The time-independent wave function is given by $\Psi(r,\theta,\phi) = C_{lm}\chi(r)Y_{lm}(\theta,\phi)$, where $\chi(r)$ is radial component of the wave function satisfying the Schrödinger equation

$$\frac{1}{r^2}\frac{d}{dr}\left(r^2\frac{d}{dr}\chi(r)\right) \left\{\frac{2\mu}{\hbar^2}[E_{lm} - V(r) + \frac{Zk_e e^2}{\epsilon_m} - \alpha_e] - \frac{l(l+1)}{r^2}\right\}\chi(r) = 0, \tag{3}$$

with μ being the electron effective mass, $V(r)$ the confining electric potential and l is orbital quantum number that indicates the angular momentum of an electron. Z represents the charge of the impurity (which is Ze, where e is the elementary charge), $Z = 1$ for hydrogenic impurities and $Z = 2$ for helium-like impurities, for example. $\hbar$ is the reduced Planck's constant and $Y_{lm}(\theta,\phi)$ are the spherical harmonics, with m being the magnetic quantum number. k_e is the Coulomb's constant and effect of the dielectric constant of the core ϵ_c has been factored in by the constant $\alpha_e = \frac{k_e^2}{\epsilon_c R_1}(\frac{\epsilon_c - \epsilon_m}{\epsilon_c \epsilon_m})$.

2.2.1 Parabolic potential

In a spherical shell, the parabolic potential can assume the mathematical representation;

$$V(r) = \left\{ \begin{array}{ll} \frac{1}{2}\mu\omega_0^2(r - R_1)^2, & \text{for } R_1 < r < R_2 \\ \infty, & elsewhere \end{array} \right\}. \tag{4}$$

ω_0 is angular frequency associated with the classical harmonic oscillator. Solution to the radial part of the Schrödinger equation is in terms of the Heun Biconfleunt function [48–51]

$$\chi(r) = C_{1lm} e^{g_1(r)} r^{|l|} H_B^+ + C_{2lm} e^{g_1(r)} r^{-|l+1|} H_B^- \tag{5}$$

with

$$H_B^{\pm} = HeunB(\pm|2l+1|, \alpha, \beta, \gamma, g_2(r))$$

and

$$\left.\begin{aligned} \alpha &= 2R_1\sqrt{\frac{\mu\omega_0}{-\hbar}} \\ \beta &= \frac{2\alpha_e - 2E_{lm}}{\hbar\omega_0} \\ \gamma &= \frac{4Zk_e e^2}{\hbar\epsilon_m}\sqrt{\frac{-\mu}{\hbar\omega_0}} \\ g_1(r) &= \frac{\mu\omega_0}{2\hbar}(r - 2R_1)r \\ g_2(r) &= -\sqrt{\frac{\mu\omega_0}{-\hbar}}r \end{aligned}\right\}. \tag{6}$$

C_{1lm} and C_{2lm} are constants obtainable from both the application of boundary conditions and normalization of the wave function. To ensure that the wave function vanishes at the walls of the quantum shell, the energy eigenvalues must be

$$E_{lm} = \alpha_e - \frac{\beta_E}{2}\hbar\omega_0 \tag{7}$$

where β_E is the value of β that satisfies the condition

$$H_B^+(R_1)H_B^-(R_2) = H_B^+(R_2)H_B^-(R_1) \tag{8}$$

where

$$H_B^{\pm}(R_{1(2)}) = HeunB(\pm|2l+1|, \alpha, \beta_E, \gamma, g_2(R_{1(2)})).$$

Without the impurity, radial component of the wave function is similar to that for the case with the impurity (Eq. (5)) with parameters being identical except for $\beta = \beta^0 = -\frac{2E^0_{lm}}{\hbar\omega_0}$ and $\gamma = 0$. This gives the energy eigenvalues in the absence of the impurity as

$$E^0_{lm} = -\frac{\beta^0_E}{2}\hbar\omega_0 \tag{9}$$

where β^0_E is the value of $\beta = \beta^0$ that satisfies the condition set in Eq. (8) but with $Z = 0$. By defining the binding energy as the energy without the impurity less that with the impurity, we have

$$BE_{lm} = \frac{1}{2}(\beta_E - \beta^0_E)\hbar\omega_0 - \alpha_e. \tag{10}$$

Shifted parabolic potential

This potential is maximum at the inner wall and decreases parabolically to a minimum (here taken as zero) at the outer wall

$$V(r) = \left\{ \begin{array}{ll} \frac{1}{2}\mu\omega_0^2(r-R_2)^2, \text{ for } R_1 < r < R_2 \\ \infty, \qquad\qquad\qquad elsewhere \end{array} \right\}. \tag{11}$$

Solution to the radial part of the Schrödinger equation is also in terms of the Heun Biconfleunt function (Eq. (5)) but with

$$\left.\begin{array}{l} \alpha = 2R_2\sqrt{\frac{\mu\omega_0}{-\hbar}} \\ g_1(r) = \frac{\mu\omega_0}{2\hbar}(r-2R_2)r \end{array}\right\} \tag{12}$$

and all other parameters being identical to those associated with the parabolic potential in the presence of the impurity. The energy spectrum, obtainable from the usual boundary conditions at the walls of the SQS, is given by Eq. (7) where β_E is the value of β that satisfies the condition set in Eq. (8), for this potential.

In the absence of the impurity, the radial component of the wave function is still expressible in terms of a combination of the Heun Biconfluent functions (Eq. (5)) with parameters identical to those for this potential in the presence of the impurity with the exception of $\beta = \beta^0 = -\frac{2E^0_{lm}}{\hbar\omega_0}$ and $\gamma = 0$. The energy eigenvalues in the absence of the impurity for a shifted parabolic potential, again, determined by the usual application of the boundary conditions, have the same form as in Eq. (9), with β^0_E being the value of $\beta = \beta^0$ that satisfies the condition stipulated in Eq. (8). One is now in a position to obtain the binding energy, given by Eq. (10), associated with this type of potential.

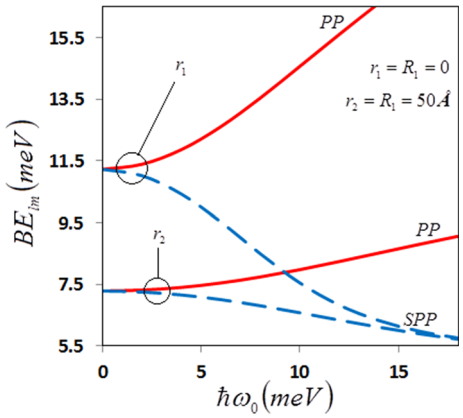

Fig. 1 The dependence of ground state binding energies on the strengths of the parabolic potential (PP) and the shifted parabolic potential (SPP) in spherical quantum structures of outer radius $R_2 = 300\mathring{A}$. The plots marked r_1 are for an inner radius $R_1 = 0\mathring{A}$ while those marked r_2 correspond to $R_1 = 50\mathring{A}$

3 Results

The variables used in the calculations are $\mu = 0.067m_e$, where m_e is the free electronic mass and $\hbar\Gamma_{fi} = 1\ meV$. The dielectric constants of the crystal and the core have been taken as $\epsilon_m = \epsilon_c = 12.5$ and the outer radius has been kept constant at $R_2 = 300\mathring{A}$. Additionally, $Z = 1$ (for hydrogen-like impurities) has been used in these results except in Fig. (5) where the photoionization cross-section associated with a hydrogen-like impurity is compared with that associated with a helium-like ($Z = 2$) impurity.

Figure 1 depicts ground state binding energies of an SQS of inner radius $r_2 = R_1 = 50\ \mathring{A}$ compared with that of an SQD ($r_1 = R_1 = 0$) as functions of strengths of the parabolic potential (PP) and the shifted parabolic potential (SPP). The outer radius of the two spherical nanostructures (the SQS and the SQD) is $R_2 = 300\mathring{A}$. The binding energies increase monotonically as the parabolic potential intensifies. This is because this potential confines electrons to a region around the inner walls, closer to the impurity. The increase in the inner radius increases the separation between the electron and the impurity, decreasing the binding energy. With the separation increased, the intensification of the parabolic potential will not displace the electrons to the same extent as for the spherical quantum dot ($R_1 = 0$), which has no restriction near or at the centre. Thus, the rate at which the binding energies increase as the potential strength increases lessens as the inner radius gets larger. The shifted parabolic potential, on the other hand, restricts the motion of electrons away from the impurity, decreasing the electrostatic interaction between the electron and the impurity. This restriction from the core can reach a degree at which the electrons become insensitive to the presence of the inner radius. Unlike for the parabolic potential, therefore, the binding energies corresponding to different inner radii

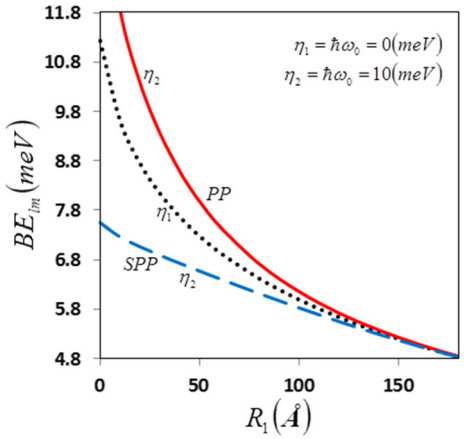

Fig. 2 The variation of ground binding energies with the inner radius of an SQS of outer radius $R_2 = 300\mathring{A}$. Dotted plot corresponds to $\hbar\omega_0 = 0$, solid plot and the dashed plot correspond to the parabolic potential (PP) and shifted parabolic potential (SPP), both of strength $\hbar\omega_0 = 10\,meV$

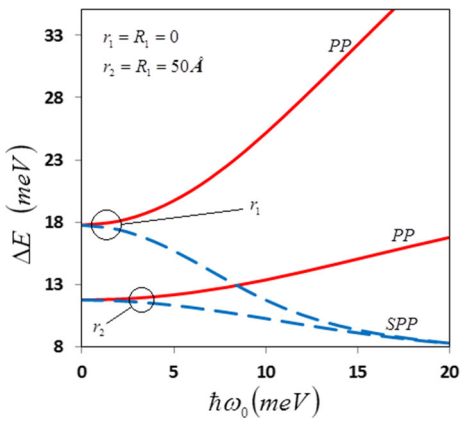

Fig. 3 Transition energies as functions of strengths of the parabolic potential (PP) and the shifted parabolic potential (SPP) in an SQS of inner radius $r_2 = R_1 = 50\mathring{A}$ and outer radius $R_2 = 300\mathring{A}$. The transition energies are compared with those of an SQD ($R_1 = 0$) of radius $R = R_2 = 300\mathring{A}$

converge as the strength of the shifted parabolic potential increases.

Figure 2 shows the dependence of ground state binding energies on the size of the inner radius of an SQS of outer radius $R_2 = 300\mathring{A}$. The three plots have been generated for $\hbar\omega_0 = 0$, and for parabolic potential (PP) and the shifted parabolic potential (SPP) each of strength $\hbar\omega_0 = 10\,meV$. Increase in the inner radius shifts the radial position expectation value of the electrons towards the outer wall, with the ground state experiencing the greatest shift. This in turn increases the electron-ion separation, decreasing the binding energy.

The dependence of transition energies on strengths of the potentials can be viewed in Fig. 3 for spherical quantum structures of outer radius $R_2 = 300\mathring{A}$ and inner radii $r_1 = R_1 = 0$ and $r_2 = R_1 = 50\mathring{A}$. The parabolic potential affects the higher l valued states than it does the lower l valued states. Consequently,

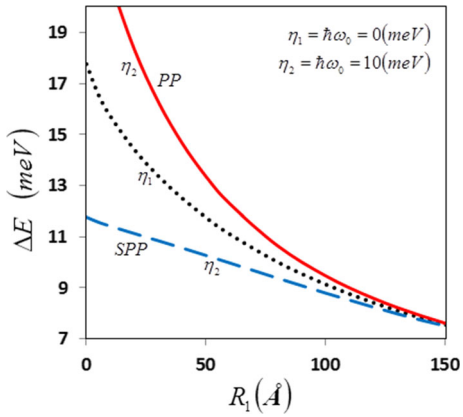

Fig. 4 The dependence of transition energies on size of the inner radius of an SQS of outer radius $R_2 = 300\mathring{A}$. The three plots have been generated for an ISSW ($\hbar\omega_0 = 0$) and for an SQS with intrinsic parabolic potential (PP) and shifted parabolic potential (SPP), both of strength $\hbar\omega_0 = 10\,meV$

increase in the strength of this potential increases transition energies. This is in contrast to the effect of the shifted parabolic potential, which tends to influence the lower l valued states more than it does the higher l valued states, consequently decreasing transition energies as it increases in strength. The presence of the inner radius increases the electron impurity distance of separation, which lowers binding energies. Additionally, the inner radius hinders the parabolic potential in confining electrons around the centre, thereby decreasing the effectiveness of the parabolic potential to increase binding energies. Thus, transition energies of SQSs of unequal inner radii diverge as strength of the parabolic potential is increased. The shifted parabolic potential, on the other hand, restricts the motion of electrons away from the inner walls, and the inner radius becomes irrelevant as the shifted parabolic potential intensifies. Consequently, transition energies of SQSs of unequal inner radii converge as strength of the shifted parabolic potential is increased.

Figure 4 shows the variation of transition energies with the inner radius of an SQS of outer radius $R_2 = 300\mathring{A}$. The dotted plots correspond to the infinite spherical square well (ISSW) ($\hbar\omega_0 = 0$), the solid curves correspond to an SQS with a parabolic potential ($\hbar\omega_0 = 10\,meV$), the dashed plots are associated with the shifted parabolic potential ($\hbar\omega_0 = 10\,meV$). Generally, the transition energies decrease as size of the inner radius increases. This is due to the fact that the inner radius affects energies of the lower l valued states more than it does the higher states, effectively decreasing the gap between energies of different l valued states.

Figure 5 shows the variation of the scaled PCS with energy of electromagnetic radiation incident on an SQS of inner and outer radii $R_1 = 50\mathring{A}$ and $R_2 = 300\mathring{A}$. The dotted line corresponds to the ISSW ($\hbar\omega_0 = 0$) while the plots marked PP and SPP are for SQSs with intrinsic parabolic and shifted parabolic potentials respectively, each of strength $\hbar\omega_0 = 10\,meV$. $Z = 1$ corresponds to PCS associated with a hydrogen-like

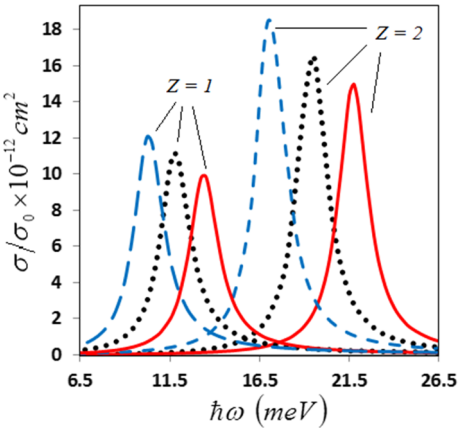

Fig. 5 The dependence of the scaled PCS on the energy of incident electromagnetic radiation for an SQS of inner and outer radii $R_1 = 50\mathring{A}$ and $R_2 = 300\mathring{A}$. The dotted line corresponds to PCS for an SQS with $\hbar\omega_0 = 0$, the solid plot corresponds to an SQS with a parabolic potential while the dashed curve is associated with an SQS with an intrinsic shifted parabolic potential, both potentials of strength $\hbar\omega_0 = 10\,meV$. $Z = 1$ corresponds to PCS associated with a hydrogenic impurity while $Z = 2$ is associated with a helium-like impurity

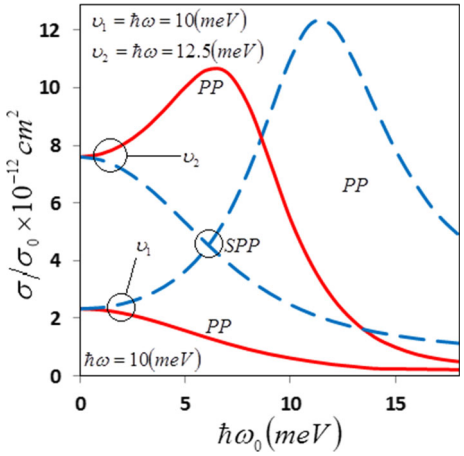

Fig. 6 The scaled PCS as a function of strengths of the parabolic potential (PP) and the shifted parabolic potential (SPP) in an SQS of inner and outer radii $R_1 = 50\mathring{A}$ and $R_2 = 300\mathring{A}$. The two pairs of plots correspond to energies of the incident electromagnetic radiation of $\nu_1 = \hbar\omega = 10\ meV$ and $\nu_2 = \hbar\omega = 12.5\,meV$

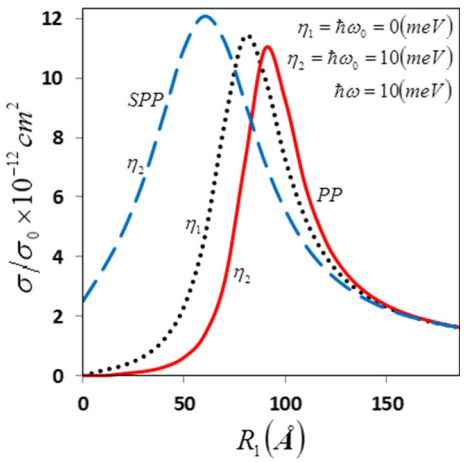

Fig. 7 The scaled PCS as a function of the inner radius of the spherical nano shell. The dotted plot is for $\eta_1 = \hbar\omega_0 = 0$, the solid plot corresponds to a parabolic potential (PP) while the dashed line corresponds to PCS for an SQS with an intrinsic shifted parabolic potential (SPP), both potentials of strength $\eta_2 = \hbar\omega_0 = 10\,meV$

impurity, while $Z = 2$ is associated with a helium-like impurity. For given dimensions of the SQS, PCS for SQS with parabolic potential are peaked at higher energies of the electromagnetic radiation than the pure ISSW. Peaks of PCS for an SQS with an intrinsic shifted parabolic potential, on the other hand, occur at radiation energies lower than for the ISSW. As mentioned already, this is because the parabolic potential enhances transition energies while the shifted parabolic potential decreases them. Another difference in the effect of these electric confining potentials is that the parabolic potential reduces the magnitude of PCS, while the shifted parabolic potential increases the magnitude of the peaks of PCS. This trend can be seen in both the hydrogen-like and the helium-like associated PCSs. PCS associated with a hydrogen-like impurity differs from that due to a helium-like impurity in at least two respects. One, the peaks of PCS associated with the helium-like impurity occurs at greater values of the photon energy than for those of the hydrogen-like impurity. Two, the magnitude of the peaks of the helium-like impurity associated PCS are greater than those of the hydrogen-like impurity associated PCS. The reason for the first distinction is increased Coulomb interaction, which perturbs the lower states more than the excited states. The reason for the second distinction is the fact that PCS varies linearly with photon energy (see Eq. (1)), and the helium-like impurity associated PCS is peaked at high photon energies, hence the larger magnitude.

The dependence of PCS on strengths of the parabolic and the shifted parabolic potentials can be viewed in Figure 6. In the figure, electromagnetic radiation of energies $\nu_1 = \hbar\omega = 10\ meV$ and $\nu_2 = \hbar\omega = 12.5\,meV$ is incident on a spherical quantum shell of inner radius $R_1 = 50\mathring{A}$ and outer radius $R_2 = 300\mathring{A}$. Solid plots (marked PP) correspond to the parabolic potential while those of the shifted parabolic potential (SPP) are represented by the dashed curves. ν_1 is less than transition energies for an ISSW ($\hbar\omega_0 = 0$) while ν_2 is greater than the ISSW transition energies. This implies that the parabolic potential can be utilized to facilitate photoionization in SQSs whose dimensions correspond to transition energies that are less than the energy of the incident electromagnetic radiation. In the case where ISSW transition energies of an SQS are more than the energy of incident radiation, then the shifted parabolic potential can be utilized to facilitate photoionization.

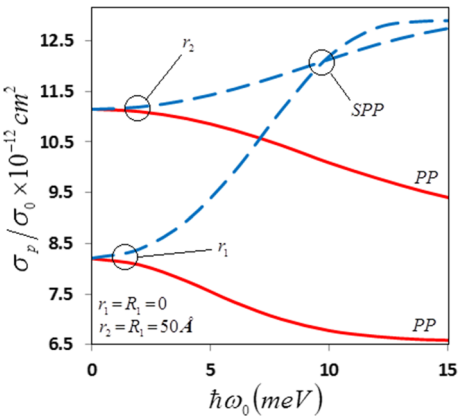

Fig. 8 Peaks of the scaled PCS as functions of strengths of the parabolic potential (PP) and the shifted parabolic potential (SPP) for an SQS of inner radius $r_2 = R_1 = 50\mathring{A}$ and outer radius of $R_2 = 300\mathring{A}$. The pair with the least intercept corresponds to an SQD ($R_1 = 0$) of radius $R = R_2 = 300\mathring{A}$

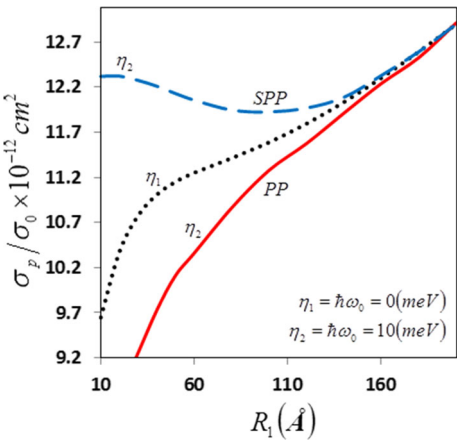

Fig. 9 Peaks of the scaled photoionization cross-section as functions of the inner radius of the spherical nano shell of outer radius $R_2 = 300\mathring{A}$. The dotted plot corresponds to the spherical quantum shell $\hbar\omega_0 = 0$, the solid plot is associated with the parabolic potential while the dashed curve corresponds to the shifted parabolic potential, each potential of strength $\hbar\omega_0 = 10\, meV$

The effect of the size of the inner radius on PCS can be viewed in Fig. 7. Here, an SQS is considered to be illuminated by an electromagnetic radiation of energy $\hbar\omega = 10\, meV$. The three figures have been generated for an SQS with $\hbar\omega_0 = 0$ (dotted plot), parabolic potential of $\hbar\omega_0 = 10\, meV$ (solid plot marked PP) and shifted parabolic of strength $\hbar\omega_0 = 10\, meV$ (dashed plot marked SPP). As can be seen in Fig. 4, transition energies decrease with increasing size of inner radius, with those corresponding to the parabolic potential (shifted parabolic potential) being higher (lower) than those of a pure ISSW ($\hbar\omega_0 = 0$). As such, for a given energy of the radiation lower than the transition energies for a solid sphere of radius $R = R_2$, photoioinization resonance will be reached for a larger (smaller) inner radius of an SQS with an intrinsic parabolic potential (shifted parabolic potential), for a constant outer radius.

Figure 8 illustrates the dependence of peaks of the PCS on the strengths of the parabolic potential (PP) and the shifted parabolic potential (SPP) for an SQS of inner and outer radii $r_2 = R_1 = 50\mathring{A}$ and $R_2 = 300\mathring{A}$. These are compared with those of an SQD ($r_1 = R_1 = 0$) of radius $R = R_2 = 300\mathring{A}$ with intrinsic parabolic potential (PP) and shifted parabolic potential (SPP). Peaks of PCS of SQSs are generally higher than those of the SQDs due to the presence of the inner radius. The inner radius restricts the motion of electrons from the centre of the nanostructure, which enhances the matrix elements between the initial state $|i\rangle$ and the final state $|f\rangle$, $\langle f|\mathbf{r}|i\rangle$.

Figure 9 depicts the dependence of the peaks of the scaled PCS on the inner radius of an SQS of outer radius $R_2 = 300\mathring{A}$. The dotted plot corresponds to the infinite spherical square well (ISSW) ($\hbar\omega_0 = 0$), the solid curve corresponds to an SQS with a parabolic potential while the dashed plot is associated with the shifted parabolic potential. It can be appreciated from the figure that as value of the inner radius approaches that of the outer radius, peaks of the PCS increase in magnitude. As the inner radius decreases, the peaks also decrease for two systems, namely ISSW and the SQS with a parabolic potential. When the inner radius is small (or zero), electrons spend most of their time at small radial distances, lowering the value of $\langle r^2\rangle$. In the case of an SQS with an intrinsic shifted parabolic potential, the motion of electrons is restricted towards the outer wall, thereby enhancing the value of $\langle r^2\rangle$. Hence, for an SQS with a shifted parabolic potential, peak of the PCS decreases only to a certain minimum after which it increases asymptotically as value of the inner radius decreases.

4 Conclusions

The effects of the geometry of confining electric potentials on the binding energies due to a donor impurity and associated photoionization cross-section in an SQS have been investigated. This has been achieved by solving the Schrödinger equation within the effective mass approximation. The geometries studied are the parabolic potential and the shifted parabolic potential, each superimposed on an infinite spherical potential well. The parabolic potential confines electrons towards the inner wall of the SQS, restricting their motion closer to the centred impurity, thereby enhancing the binding energies as the electric potential intensifies. The shifted parabolic potential, on the other hand, restricts the motion of electrons away from the inner wall, consequently increasing the electron-impurity separation, thereby decreasing the binding energies. The other parameter that increases the electron-impurity separation is the inner radius, which lowers the binding energy as it increases. Results show that these two potentials drastically modify PCS mainly in two ways.

First is that the parabolic potential blueshifts peaks of PCS while the shifted parabolic potential redshifts the peaks. The second is that the parabolic potential decreases the magnitude of the peaks of the PCS while the shifted parabolic potential increases the magnitudes of the peaks. This is crucial for nanotechnology as it gives control over ways of modifying quantum quantities like binding energies and PCS for nanodevice applications.

Author contributions

MT: Conceptualization of this study, obtaining solutions, writing - original draft preparation and simulation. LKS: Validation, reviewing and editing. SP: Writing, reviewing and editing. All the authors have read and approved the final manuscript.

Data Availability Statement This manuscript has no associated data or the data will not be deposited. [Authors' comment: Results were obtained using Maple mathematical software.]

References

1. P. Chen, J. Wang, Y. Lu, S. Zhang, X. Liu, W. Hou, Z. Wang, L. Wang, The fabrication of res2 flowers at controlled locations by chemical vapor deposition. Physica E **89**, 115–118 (2017). https://doi.org/10.1016/j.physe.2017.02.004
2. L. Meng, J. Feng, Y. Yu, W. Yan, H. Li, X. Wang, and X. Yan. Formation mechanism of 2d ws2 with different morphology by chemical vapor deposition. *Physica E*, 114(113641) (2019). https://doi.org/10.1016/j.physe.2019.113641
3. D. Cho, J. Park, T. Kim, S. Jeon, Recent advances in lithographic fabrication of micro-/nanostructured polydimethylsiloxanes and their soft electronic applications. J. Semiconductors **40**(11), 111605 (2019). https://doi.org/10.1088/1674-4926/40/11/111605
4. S. Rasappa, H. Hulkonen, L. Schulte, S. Ndoni, J. Reuna, T. Salminen, T. Niemi, High molecular weight block copolymer lithography for nanofabrication of hard mask and photonic nanostructures. J. Colloid Interface Sci. **534**, 420–429 (2019). https://doi.org/10.1016/j.jcis.2018.09.040
5. R. R. Reznik, K. P. Kotlyar, N. V. Kryzhanovskaya, S. V. Morozov, and G. E. Cirlin (2019) Synthesis by molecular beam epitaxy and properties of ingan nanostructures of branched morphology on a silicon substrate. Tech. Phys. Lett., 45(1111-1113). https://doi.org/10.1134/S1063785019110129
6. Q. Sun, H. Gao, X. Yao, K. Zheng, P. Chen, W. Lu, J. Zou, Au-catalysed free-standing wurtzite structured inas nanosheets grown by molecular beam epitaxy. Nano Res. **12**(11), 2718–2722 (2019). https://doi.org/10.1007/s12274-019-2504-7
7. F. Dvorak, R. Zazpe, M. Krbal, H. Sopha, J. Prikryl, S. Ng, L. Hromadko, F. Bures, J.M. Macak, One-dimensional anodic tio2nanotubes coated by atomic layer deposition: towards advanced applications. Appl. Materials Today **14**, 1–20 (2019). https://doi.org/10.1016/j.apmt.2018.11.005
8. E. Janik, A. Wachnicka, E. Guziewicz, M. Godlewski, S. Kret, W. Zaleszczyk, E. Dynowska, A. Presz, G. Karczewski, T. Wojtowicz, Znte-zno core-shell radial heterostructures grown by the combination of molecular beam epitaxy and atomic layer deposition. Nanotechnology **21**, 015302 (2010)
9. X.-E. Zhang, Nanobiology-symphony of bioscience and nanoscience. Sci China Life Sci **63**(8), 1099–1102 (2020). https://doi.org/10.1007/s11427-020-1741-y
10. Y. He, C. Fen, S.-T. Lee, Silicon nanostructures for bioapplications. Nano Today **5**, 282–295 (2010)
11. S Gunalan, R Sivaraj, Rajendran V. Green synthesized zno nanoparticles against bacterial and fungal pathogens. *Prog. Nat. Sci.*, 22:693–700 (2012)
12. H. Chen, H. Liu, Z. Zhang, K. Hu, X. Fang, Nanostructured photodetectors: from ultraviolet to terahertz. Adv. Mater. **28**, 403–433 (2016). https://doi.org/10.1002/adma.201503534
13. Y. Fu, H. Zhu, J. Chen, M. P. Hautzinger, X.-Y. Zhu, S. Jin, Metal halide perovskite nanostructures for optoelectronic applications and the study of physical properties. *Nature Reviews. Materials*, 4(3) (2019). https://doi.org/10.1038/s41578-019-0080-9
14. J. Jie, W. Zheng, I. Bello, C.-S. Lee, S.-T. Lee, One-dimensional ii–vi nanostructures: synthesis, properties and optoelectronic applications. Nano Today **5**, 313–336 (2010)
15. A.B. Djurišić, A.M.C. Ng, X.Y. Chen, Zno nanostructures for optoelectronics: material properties and device applications. Prog. Quant. Electron. **34**, 191–259 (2010)
16. I. Llatser, C. Kremers, A. Cabellos-Aparicio, M. Jornet J, D.N. Chigrin, E. Alarcón, Graphene-based nanopatch antenna for terahertz radiation. *Photonics and Nanostruct.*, 10:353–358 (2012)
17. A.L.M. Reddy, S.R. Gowda, M.M. Shaijumon, P.M. Ajayh, Hybrid nanostructures for energy storage applications. Adv. Mater. **24**, 5045–5064 (2012)
18. J. Jiang, Y. Li, J. Liu, C. Yuan, X. Huang, X.W. (D) Lou, Recent advances in metal oxide-based electrode architecture design for electrochemical energy storage. *Adv. Mater.*, 24:5166–5180 (2012)
19. E. Stratakis, E. Kymakis, Nanoparticle-based plasmonic organic photovoltaic devices. Mater. Today **16**, 133–146 (2013)
20. A.K. Menon, B.K. Kupta, Nanotechnology: a data storage perspective. *Nanostruct. Mater.*, 11:965–986 (1999)
21. P. Lodahl, Quantum-dot based photonic quantum networks. Quantum Sci. Technol. **3**, 013001 (2018). https://doi.org/10.1088/2058-9565/aa91bb
22. I. Cesar, A. Kay, J.A.G. Martinez, M. Grätzel, Translucent thin film fe_2o_3 photoanodes for efficient water splitting by sunlight: nanostructure-directing effect of si-doping. J. Am. Chem. Soc. **128**, 4582–4583 (2006)
23. S. Maldonado, S. Morin, K.J. Stevenson, Structure, composition, and chemical reactivity of carbon nanotubes by selective nitrogen doping. Carbon **44**, 1429–1437 (2006)
24. Y. Shao, J. Sui, G. Yin, Y. Gao, Nitrogen-doped carbon nanostructures and their composites as catalytic materi-

als for proton exchange membrane fuel cell. Appl. Catal. B-Environ. **79**, 89–99 (2008)
25. E.B. Al, E. Kasapoglu, S. Sakiroglu, C.A. Duque, I. Sökmen, Binding energy of donor impurity states and optical absorption in the tietz-hua quantum well under an applied electric field. J. Mol. Struct. **1157**, 288–291 (2018). https://doi.org/10.1016/j.molstruc.2017.12.068
26. M. Hu, H. Wang, Q. Gong, S. Wang, External electric field effect on the binding energy of a hydrogenic donor impurity in ingaasp/inp concentric double quantum rings. Int. J. Modern Phys. B **32**(11), 1850138 (2018). https://doi.org/10.1142/S0217979218501382
27. A.L. Vartanian, A.L. Asatryan, A.A. Kirakosyan, K.A. Vardanyan, Influence of image charge effect on the binding energy of hydrogen-like donor impurity in a near-surface quantum well under transverse electric field. Physica E **106**, 1–4 (2019). https://doi.org/10.1016/j.physe.2018.10.022
28. S. Pratap, Transmission and ldos in case of zgnr with and without magnetic field. Superlattice. Microst. **104**, 540–546 (2017). https://doi.org/10.1016/j.spmi.2017.02.046
29. E Kasapoglu. Sari, H. Sökmen I, Binding energy of impurity states in an inverse parabolic quantum well under magnetic field. *Physica B*, 390:216–219 (2007)
30. E.M. Kazaryan, A.V. Meliksetyan, L.S. Petrosyan, H.A. Sarkisyan, Impurity states of narrow-gap semiconductor parabolic quantum dot in the presence of extremely strong magnetic field. Physica E **31**, 228–231 (2006)
31. E. Kasapoglu, H. Sari, I. Sökmen, Density of impurity states of hydrogenic impurities in an inverse parabolic quantum well under the magnetic field. *Physica B*, 392:213–216 (2007)
32. S. Elagoz, P. Başer, U. Yahşi, The magnetic field dependency of hydrogenic impurity binding energy under inverse lateral parabolic potential. Physica B **403**, 3879–3882 (2008)
33. E. C. Niculescu, C. Stan, G. Tiriba, and Truşcă C. Magnetic field control of absorption coefficient and group index in an impurity doped quantum disc. *Eur. Phys. J. B*, 90:100 (2017) https://doi.org/10.1140/epjb/e2017-80138-0
34. Effects of hydrostatic pressure and an intense laser, A Miguez, R Franco, and Silva-Valencia J. Donor and acceptor states in gaas-(ga, al)as quantum dots. Int. J. Mod. Phys. B **24**, 5761–5770 (2010)
35. M. Santhi, A.J. Peter, C. Yoo, Hydrostatic pressure on optical absorption and refractive index changes of a shallow hydrogenic impurity in a gaas/gaalas quantum wire. Superlattice. Microst. **52**, 234–244 (2012)
36. E. Sadeghi, A. Avazpour, Binding energy of an off-center donor impurity in ellipsoidal quantum dot with parabolic confinement potential. Physica B **406**, 241–244 (2011)
37. L. Dong-Ming, X. Wen-Fang (2009) Binding energy of an off-center d^- in a spherical quantum dot. *Commun. Theor. Phys.(Beijing, China)*, 51:919–922
38. M. Cristea, E.C. Niculescu, Off-center shallow donors in a spherical si quantum dot with dielectric border. Int. J. Quantum Chem. **112**, 1737–1745 (2011)
39. C.-Y. Hsieh, Lower lying states of hydrogenic impurity in a multi-layer quantum dot. Chinese J. Phys. **38**, 478–490 (2000)
40. S. Aktas, F.K. Boz, The binding energy of hydrogenic impurity in multilayered spherical quantum dot. Physica E **40**, 753–758 (2008)
41. H. Taş, M. Şahin, The electronic properties of a core/shell/well/shell spherical quantum dot with and without a hydrogenic impurity. J. Appl. Phys. **111**, 083702 (2012)
42. S. M'zerd, M. El Haouari, M. Aghoutane, M. El-Yadri, E. Feddi, F. Dujardin, I. Zorkani, A. Jorio, M. Sadoqi, and G. Long. Electric field effect on the photoionization cross section of a single dopant in a strained *alas/gaas* spherical core/shell quantum dot. *J. Appl. Phys.*, 124:164303, 2018. https://doi.org/10.1063/1.5046859
43. L. Shi, Z.W. Yan, Stark shift and photoionization cross section of on-center and off-center donor impurity in a core/shell ellipsoidal quantum dot. Physica E **98**, 111–117 (2018). https://doi.org/10.1016/j.physe.2017.12.034
44. E. Feddi, M. El-Yadri, F. Dujardin, R.L. Restrepo, C.A. Duque, Photoionization cross section and binding energy of single dopant in hollow cylindrical core/shell quantum dot. J. Appl. Phys. **121**, 064303 (2017). https://doi.org/10.1063/1.4975648
45. E. Iqraoun, A. Sali, A. Rezzouk, E. Feddi, F. Dujardin, M.E. Mora-Ramos, C.A. Duque, Donor impurity-related photoionization cross section in gaas cone-like quantum dots under applied electric field. Philosophical Mag. **97**(18), 1445–1463 (2017). https://doi.org/10.1080/14786435.2017.1302613
46. M. Tshipa, The effects of cup-like and hill-like parabolic confining potentials on photoionization cross section of a donor in a spherical quantum dot. Eur. Phys. J. B **89**, 177 (2016). https://doi.org/10.1140/epjb/e2016-60988-6
47. M. Tshipa (2017) Photoionization cross section in a spherical quantum dot: Effects of some parabolic con1ning electric potentials. *Condensed Matter Physics, , Vol.*, 20(2): 23703: 1-9 https://doi.org/10.5488/CMP.20.23703
48. E.R. Arriola, A. Zarzo, J.S. Dehesa, Spectral properties of the biconfluent heun differential equation. J. Comput. Appl. Math. **37**, 161–169 (1991)
49. A. Roseau, On the solutions of the biconfluent heun equations. Bull. Belg. Math. Soc. **9**, 321–342 (2002)
50. S. Belmehdi, J.-P. Chehab, Integral representation of the solutions to the heun's biconfluent equation. Abstr. Appl. Anal. **4**, 295–306 (2004)
51. E.S. Cheb-Terrab, Solutions for the general, confluent and biconfluent heun equations and their connection with abel equations. J. Phys. A: Mth. Gen. **37**, 9923–9949 (2004)